Water Science & Technology

IWA PUBLISHING

Water Science & Technology Vol 88 No 6, 1564 doi: 10.2166/wst.2023.272

Comparative study of zinc oxide nanocomposites with different noble metals synthesized by biological method for photocatalytic disinfection of *Escherichia coli* present in hospital wastewater

Pankaj Kumar Jha[a], Chonlada Pokhum[b], Pichai Soison[b,c], Kua-anan Techato[a] and Chamorn Chawengkijwanich[b,*]

[a] Department of Sustainable Energy Management, Faculty of Environmental Management, Prince of Songkla University, Hat Yai, Songkla 90110, Thailand
[b] National Nanotechnology Center, National Science and Technology Development Agency, 111 Thailand Science Park, Phahonyothin Road, Pathum Thani 12120, Thailand
[c] School of Energy, Environment and Materials, King Mongkut's University of Technology Thonburi, Pracha Uthit Road, Bang Mod, Bangkok 10140, Thailand
*Corresponding author. E-mail: chamorn@nanotec.or.th

CC, 0000-0003-4601-1365

ABSTRACT

Binary zinc oxide (ZnO) nanocomposites with different noble metals, silver (Ag) and ruthenium (Ru), were prepared from an aqueous leaf extract of *Callistemon viminalis*. The biosynthesized photocatalysts were characterized and examined for their photocatalytic disinfection against *Escherichia coli* isolated from hospital wastewater. The influence of the different noble metals showed a difference in physicochemical characteristics and photocatalytic efficiency between Ag–ZnO and Ru–ZnO. The photocatalytic degradation of methylene blue and photocatalytic disinfection were found to be in the order Ag–ZnO > Ru–ZnO > ZnO. The photocatalytic disinfection of Ag–ZnO reached a 75% reduction in 60 min, compared to 34 and 9% reductions of Ru–ZnO and ZnO, respectively. The kinetic reaction rate for the photocatalytic disinfection of Ag–ZnO was found to be 2.8 times higher than that of Ru–ZnO. The outstanding photocatalytic activity of Ag–ZnO over Ru–ZnO was attributed to higher crystallinity, greater UVA adsorption capacity, smaller particle size, and the additional antimicrobial effect of Ag itself. The *C. viminalis*-mediated Ag–ZnO nanocomposites can be a potential candidate for photocatalytic disinfection of drug-resistant *E. coli* in hospital wastewater.

Key words: biosynthesis, hospital wastewater, photocatalyst, ruthenium, silver, zinc oxide

HIGHLIGHTS

- Biosynthesis and characterization of two zinc oxide-based nanocomposites with silver and ruthenium were presented.
- Photocatalytic disinfection of *Escherichia coli* present in hospital wastewater was demonstrated.
- The influence of different noble metals (silver and ruthenium) on the characteristics and photocatalytic efficiency were discussed.

1. INTRODUCTION

The pollution of natural water by chemical and biological contaminants is being recognized as a major global concern. These pollutants are highly hazardous not only to the health of humans but also to the entire ecosystem. Moreover, there has been a growing occurrence of antibiotic-resistant bacteria in water sources (Odonkor & Addo 2018). The prevalence of multidrug-resistant *Escherichia coli* in water sources is reported as 49.48% among other species. In addition, *E. coli* is susceptible to almost all antimicrobial agents, but it has a great capacity to accumulate antimicrobial resistance genes (Abu-Sini *et al.* 2023). Multidrug resistance in *E. coli* has become a worrying issue and is increasingly observed (Poirel *et al.* 2018). Hospital wastewater acts as a reservoir for antibiotic resistance genes rather than other wastewater systems (Zhang *et al.* 2020).

Advanced oxidation processes (AOP) are one of the most effective methods for the elimination of organic compounds and bacteria from water and wastewater by oxidation (Sadeghfar *et al.* 2021). This is due to the fact that these processes mainly use hydroxyl radicals (˙OH), which have a high oxidation potential, for the remediation of organic contaminants and hazardous pollutants into carbon dioxide and water. Photocatalysis is a heterogeneous AOP process using ultraviolet (UV) light irradiation and a semiconductor photocatalyst to produce ˙OH radicals, which has been an eco-friendly process for the

removal of organic pollutants from water (Ahmed & Haider 2018), especially emerging contaminants such as pharmaceutical and personal care products (Çifçi *et al.* 2016; Oluwole *et al.* 2020). Several metal oxide materials have been used as photocatalysts, such as titanium dioxide (TiO_2) and zinc oxide (ZnO), to accelerate the degradation and disinfection of chemical and biological compounds (Roy & Chakraborty 2021; Shintre *et al.* 2022). ZnO nanoparticles have shown some additional advantages, such as being relatively non-toxic, cheap, safe, biocompatible, and easily available, which has allowed them to be widely used in photocatalytic and biological applications (Moezzi *et al.* 2012).

Generally, when ZnO is irradiated with UV light at a wavelength less than 385 nm, electrons in the valence band (VB) jump to the conduction band (CB), subsequently producing positive holes (h^+) and electrons (Moezzi *et al.* 2012). The VB holes react with the water molecules and hydroxide ions to form hydroxyl ($^{\bullet}OH$) radicals, whereas the electron reacts with oxygen molecules and forms superoxide anion ($^{\bullet}O_2^-$) radicals. The $^{\bullet}OH$ radical is a powerful oxidizing agent that reacts with and decomposes most organic compounds. However, ZnO has a fast recombination of photoinduced electron and hole pairs, which in turn reduces its photocatalytic efficiency (Nagaraju *et al.* 2017). Therefore, many studies have been focused on the hybridization of ZnO with noble metals to improve charge separation, thereby increasing the photocatalytic activity of ZnO (Bloh *et al.* 2014; Liu *et al.* 2017; Nagaraju *et al.* 2017; Manríquez *et al.* 2018; Pathak *et al.* 2019; Shintre *et al.* 2022). These active noble metals for modification of ZnO, for example, are silver (Ag), ruthenium (Ru), palladium (Pd), and gold (Au). Most reports have paid more attention to the comparison of the photocatalytic activity between pure ZnO and metal-modified ZnO (Bloh *et al.* 2014; Adeel *et al.* 2021; Shintre *et al.* 2022). However, it is worthwhile studying the influence of different noble metals on metal-modified ZnO. The catalytic activity of noble metal-ZnO nanostructures has been found to rely on not only the species of noble metal but also the architecture of the catalyst material (Liu *et al.* 2017).

Pathak *et al.* (2019) have reported that the morphology and optical properties of Pd-doped ZnO, Au-doped ZnO, and Ag-doped ZnO were similar, whereas Ag–ZnO provided higher antimicrobial activity and a lower minimum inhibitory concentration (MIC) than the others. This is due to the strong antimicrobial effect of Ag. On the other hand, RuO_2 has been studied as a catalyst showing strong oxidation and antimicrobial properties (Kannan & Sundrarajan 2015; Manríquez *et al.* 2018). However, Ag–ZnO and Ru–ZnO have not been studied comparatively yet. Typically, the synthesis of ZnO and ZnO nanocomposites utilizes chemical methods. In recent years, green synthesis has attracted significant attention as a simple, cost-effective, and eco-friendly alternative route to conventional chemical and physical methods for the preparation of nanoparticles and metal oxides. Bioactive constituents in plant extracts are utilized as natural reducing, stabilizing, and capping agents for synthesizing nanoparticles (Basnet *et al.* 2018).

Callistemo viminalis, commonly known as bottlebrush, is widely distributed across the world. It has been reported to have medical importance, such as antibacterial, antifungal, antioxidant, and other pharmaceutical and insecticidal properties (Ahmad & Athar 2017). *C. viminalis (CV)* extract is rich in phenolics and flavonoids (Salem *et al.* 2017), which are involved in the stabilization, formation, and bioreduction of metal oxides and metal nanoparticles (Basnet *et al.* 2018). In this research, two ZnO-based nanocomposites with different noble metals (Ag and Ru) were prepared by green synthesis. The leaf extract of CV was used as a bio-reducing agent for nanoparticle formation through a precipitation process. The characteristics, photocatalytic disinfection, and degradation efficiencies of silver–zinc oxide (Ag–ZnO) and ruthenium–zinc oxide (Ru–ZnO) nanocomposites were studied. The photocatalytic disinfection was tested against *Escherichia coli* present in hospital wastewater, while the photocatalytic degradation was evaluated using methylene blue (MB) dye. MB is widely used in hospital activities for various diagnostic and therapeutic purposes (Muttaqin *et al.* 2022); thus, it has been reported as a hospital wastewater model pollutant as well. The novelty of this work was to reveal the influence of different noble metal incorporation on the physicochemical properties and photocatalytic performance between Ag–ZnO and Ru–ZnO nanocomposites.

2. METHODS

2.1. Materials

Zinc nitrate hexahydrate ($Zn(NO_3)_2{\cdot}6H_2O$), ruthenium (III) chloride (RuCl3), and silver nitrate ($AgNO_3$), provided by Sigma-Aldrich (St. Louis, MO, USA), and sodium hydroxide (NaOH) pellets from Carlo Erba, France, were applied, respectively, as precursors and precipitating agents for the synthesis process. MB was purchased from Sigma Aldrich, USA. Nutrient agar (NA), Muller–Hilton agar (MHA), and peptone were purchased from Difco Laboratories, USA. All the chemicals used were of analytical grade, and all solutions were prepared in deionized (DI) water.

2.2. Leaf extraction

The fresh leaves of CV were collected from a local garden. Later, they were cleaned with DI water, air-dried for 48 h, and cut into small pieces. To produce the extract, 30 g of the small leaf pieces were added to 250 mL of DI water and heated at 60 °C for 20 min. Then, the aqueous extract was cooled down and filtered through Whatman filter paper no. 1. The obtained extract (a pale yellow) was kept in a refrigerator at 4 °C for experimentation.

2.3. Photocatalysts preparation

The pure ZnO, Ag–ZnO, and Ru–ZnO nanocomposites were synthesized via a precipitation method using CV extract. Zinc nitrate hexahydrate ($Zn(NO_3)_2{\cdot}6H_2O$), ruthenium (III) chloride ($RuCl_3$), and silver nitrate ($AgNO_3$) were used as Zn, Ru, and Ag precursors, respectively, and prepared in DI water.

To synthesize ZnO nanoparticles (NPs), a solution (100 mL) containing 70 mM zinc nitrate was mixed with 10 mL of CV leaf extract under stirring. The solution was then adjusted to pH 12 by adding 1 M NaOH dropwise. Next, the reaction solution was heated to 60 °C and kept under constant stirring for several hours until the color of the solution stopped changing further. The precipitates settled at the bottom of the beaker. After this, the system was allowed to cool down to room temperature. The supernatant was discarded, and the precipitates were collected and air-dried for 24 h. Lastly, they were thoroughly ground into a fine powder and calcined for 3 h at 300 °C.

Similarly, the same synthesis procedure was used to synthesize Ag–ZnO and Ru–ZnO nanocomposites. 100 mL of 1 mM $AgNO_3$ solution and 1 mM $RuCl_3$ solution were added as the Ag and Ru precursors to the reaction solution. The mass percentages of the Ag and Ru elements for the Ag–ZnO and Ru–ZnO synthesis were determined to be 5% Ag w/v and 5% Ru w/v, respectively. Figure 1 illustrates the synthesis process of pure ZnO, Ag–ZnO, and Ru–ZnO using leaf extract. The resulting powders of ZnO, Ag–ZnO, and Ru–ZnO nanocomposites displayed off-white, black, and blue colors, respectively.

2.4. Characterization

The effect of different noble metals on the ZnO-based nanocomposites was determined using various advanced techniques. Fourier transform infrared spectrometry (FTIR) was performed with a Shimadzu IRTracer-100AH FTIR in attenuated total reflectance (ATR) mode in the range of 4,000–400 cm^{-1}. A powder X-ray diffraction (XRD) instrument, the Bruker D8-Advance, with Cu Kα radiation, $\lambda = 1.5417$ Å, was used to study the crystal structures of nanomaterials. The average crystallite size of the synthesized ZnO, Ag–ZnO, and Ru–ZnO nanocomposites was calculated using Debye–Scherrer's equation

Figure 1 | Schematic diagram of the green synthesis process using *C. viminalis* (CV) extract to obtain ZnO, Ag–ZnO, and Ru–ZnO.

(Equation (1)) (Faisal *et al.* 2021):

$$D = \frac{k\lambda}{\beta}\cos\ \theta \tag{1}$$

where D represents the half peak height of an XRD line due to a specific crystalline plane, k denotes the shape factor (0.94), λ depicts the X-ray wavelength of 1.5417 Å, and β and θ refer to the full width at half maximum (FWHM) in radians and Bragg's angle, respectively. The JEM 2100 transmission electron microscopy (TEM, JEOL, Japan) and field emission scanning electron microscope (FESEM, Hitachi SU-8030) images were acquired to investigate the morphology and size of samples. Selected area electron diffraction (SAED) patterns were analyzed using TEM for two-dimensional (2D) electron diffraction of samples. The chemical compositions of each sample were obtained using energy-dispersive X-ray spectroscopy (EDS, EDAX, AMETEK, Inc.). The UV-Vis absorption spectra were measured on a UV-Vis spectrophotometer (model Lambda 650, Perkin Elmer, USA) from 200 to 800 nm.

2.5. Photocatalytic activity test

Biosynthesized ZnO, Ag–ZnO, and Ru–ZnO were evaluated for their photocatalytic degradation of MB dye under UVA irradiation. The procedure was carried out with photocatalyst powders according to Nagaraju *et al.* (2017), with slight modifications. All experiments were carried out in a homemade UVA chamber equipped with four 18-watt black light lamps (UV-A, Philips) at 25 °C. In a typical procedure, 100 mg of photocatalysts were added to 100 mL of MB aqueous solution (MB concentration of 10 mg/L) in a glass beaker. Before irradiation, the solution was magnetically stirred in the dark for 120 min to ensure the establishment of an adsorption–desorption equilibrium. Then, the mixture reaction was magnetically stirred under UVA irradiation for 200 min. The distance between the light source and the sample was maintained at 10 cm. Figure 2 schematically demonstrates the photocatalytic reactor used in this work. The sample (2.5 mL) of the suspension was withdrawn from the reaction mixture at 40-min intervals. The dispersed ZnO, Ag–ZnO, and Ru–ZnO photocatalysts were removed using a microcentrifuge. The change in MB concentration was monitored by UV-visible spectroscopy (Perkin Elmer, model Lambda 650) at 664 nm wavelength.

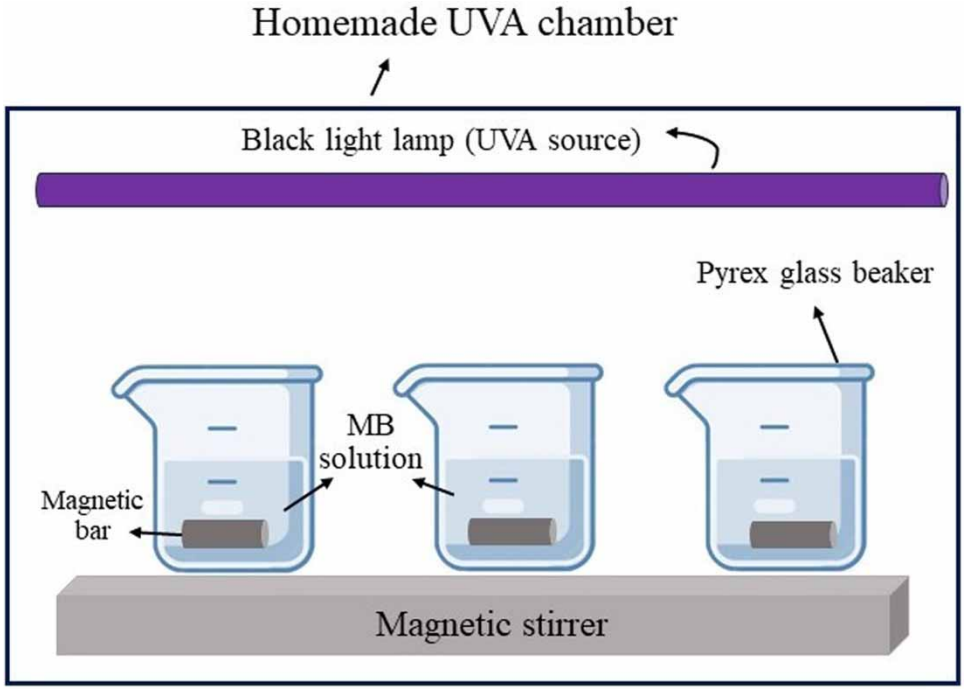

Figure 2 | The experimental set up used in photocatalytic MB degradation.

The percent degradation (%) of the degraded MB dye was calculated by Equation (2). The degradation kinetics was followed using a pseudo-first-order reaction (Equation (3)):

$$\% = \frac{C_0 - C_t}{C_0} \times 100 \quad (2)$$

$$\ln\left(\frac{C_0}{C_t}\right) = kt \quad (3)$$

where C_0 and C_t are the initial concentration and concentration after t time intervals, and k is the apparent reaction rate constant.

2.6. Isolation of *E. coli* present in hospital wastewater

The wastewater sample was gathered from the wastewater treatment plant of Songklanagarind Hospital (Songkhla, Thailand). *E. coli* was isolated from wastewater, according to Maal *et al.* (2015). One liter of wastewater was filtered through a nitrocellulose filter (pore size 0.22 μm). The filtrate was mixed into 500 mL of nutrient broth medium (HiMedia Laboratories Pvt. Ltd, Mumbai, India) and incubated for 24 h. After incubation, the nutrient broth medium containing cultured bacteria was streaked on MacConkey agar (Becton, Dickson, and Company, USA) and incubated for 24 h. The pink colonies were observed and collected from the MacConkey agar, and they were re-streaked on eosin methylene blue (EMB) agar (HiMedia Laboratories Pvt. Ltd, India). *E. coli* bacteria were found in the metallic green sheen colonies on EMB agar (Maal *et al.* 2015). A single colony of *E. coli* was picked, and it was subcultured in NA media (HiMedia Laboratories Pvt. Ltd). Isolated *E. coli* from NA plates was transferred to LB broth and incubated at 37 °C overnight for use in further experiments.

2.7. Photocatalytic disinfection of *E. coli* present in hospital wastewater

The photocatalytic disinfection of biosynthesized ZnO, Ag–ZnO, and Ru–ZnO was evaluated against *E. coli* present in hospital wastewater. The suspensions of pure ZnO, Ag–ZnO, and Ru–ZnO were prepared at concentrations of 1 mg/mL). For this, 10 mL of *E. coli* stock suspension was added to the flask containing 90 mL of a 0.9% saline solution and incubated for 2 h. Subsequently, 100 mL of bacterial solution was taken and added to 900 mL of the sterile DI water to form the stock solution (2.03×10^7 CFU/mL). Next, 1 mL of pure ZnO, Ag–ZnO, and Ru–ZnO suspensions (1 mg/mL) were added to 99 mL of the *E. coli* solution. The final concentration of biosynthesized nanomaterials in the *E. coli* solution was 1 mg/100 mL. The suspension was constantly stirred and subjected to UVA illumination for 60 min at 25 °C. An aliquot (3 mL) of the suspension was taken at 15-min intervals and immediately diluted to an appropriate dilution. The diluted samples were spread on NA and incubated at 37 °C for 24 h. The number of colonies formed was counted to determine the number of viable cells. All the above experiments were conducted in triplicate. The percentage of disinfection (%) was determined by Equation (2). The disinfection kinetics was described by a pseudo-first-order reaction using Equation (3).

2.8. Antimicrobial test against *E. coli* present in hospital wastewater

The agar disc diffusion assay was carried out to evaluate the antibacterial properties of the biosynthesized ZnO, Ag–ZnO, and Ru–ZnO. Initially, an isolated *E. coli* inoculum (2.8×10^7 CFU/mL) was spread on the MHA agar plate, and then sterile discs loaded with 40 μL of pure ZnO, Ag–ZnO, and Ru–ZnO suspensions (two concentrations of 1 and 10 mg/mL) were placed on the MHA plates. The plates were then incubated at 37 °C. After 24 h, the inhibition zone formed around each disc was measured. Tests were performed in triplicate.

2.9. Immobilized ZnO and ZnO-based nanocomposite onto filter paper

The microbial reduction efficiency of ZnO, Ag–ZnO, and Ru–ZnO was further determined using a standard test method (ISO 27447:2019 Test Method for Antibacterial Activity of Semiconducting Photocatalytic Materials). For this, 2 g of ZnO, Ag–ZnO, and Ru–ZnO were dispersed in 100 mL of sterile DI water using ultrasonication to give a uniform suspension. Subsequently, the dispersed suspension (1 mL) was drop-coated onto the surface of the filter paper (Whatman no. 1, 5 × 5 cm) and allowed to dry at 100 °C for 30 min. The determined concentration of ZnO, Ag–ZnO, and Ru–ZnO on the coated paper was 0.8 mg/cm^2. The antimicrobial activity was performed by pouring about 1 mL (4×10^4 CFU/mL) on the photocatalyst-coated and noncoated papers and then covering them with a glass coverslip. Next, the samples were placed in the

absence or presence of UVA irradiation for 8 h. After the desired time, the paper specimens were washed with sterile DI water and immediately diluted. The density of living cells was then also determined by counting the CFU/mL on NA.

3. RESULTS AND DISCUSSION

3.1. Biosynthesis of ZnO, Ag–ZnO, and Ru–ZnO

The leaf extract of CV is reported to be rich in polyphenols and flavonoids (Salem *et al.* 2017). Polyphenolic compounds, mainly phenolic acids, present in the CV extract acted as both reducing and stabilizing agents to synthesize nanoparticles (Dwivedi *et al.* 2021). The presence of OH groups in flavonoids and phenolic compounds is responsible for the reduction of metal ions into nanoparticles, and the C = O – C, C = C, and C = O groups in leaf extract may act as stabilizers (Basnet *et al.* 2018).

In the present work, Zn^{2+}, Ag^{+}, and Ru^{3+} ions were reduced into ZnO, Ag–ZnO, and Ru–ZnO particles. The color of the mixture was changed, which confirmed the formation of nanoparticles (Figure 1). When the color stopped changing further, the bioreduction of metal ions into nanoparticles was complete. The difference in color appearance between pure ZnO and ZnO-based nanocomposites was observed. ZnO is naturally white. Conversely, the presence of Ag nanoparticle aggregates and high Ag loading can be responsible for the black color of the Ag–ZnO nanocomposite. The black color of Ag–ZnO indicates the strong absorption of visible light (Choi *et al.* 2015). For the Ru–ZnO nanocomposite, $RuCl_3$ was used as a Ru precursor in the biosynthesis of Ru–ZnO. Ru^{3+} ions could enter the ZnO lattice, whereas excess Ru^{3+} ions can be oxidized to Ru^{4+}, leading to the formation of RuO_2 nanograins (Aranganayagam *et al.* 2013). The presence of RuO_2 can be observed in the XRD result (Figure 3). Nevertheless, the presence of RuO_2 might not account for the blue coloration of the Ru–ZnO nanocomposite, as RuO_2 is black. Bloh *et al.* (2014) reported that Ru species defects in the ZnO lattice contributed to the color of Ru-modified ZnO.

3.2. X-ray diffraction

The XRD analysis of ZnO, Ag–ZnO, and Ru–ZnO nanocomposites prepared using CV extract (Figure 3) reveals ZnO in a hexagonal wurtzite structure. The diffraction pattern clearly shows peaks corresponding to ZnO located at 31.65°, 34.32°, 36.00°, 47.49°, 56.46°, 62.83°, 66.32°, 67.83°, 69.00°, 72.5°, and 77°, which corresponded to crystal faces of (100), (002), (101), (102), (110), (103), (200), (112), (201), (004), and (202) planes. The sharp and strong peaks of the XRD patterns showed that the prepared ZnO, Ag–ZnO, and Ru–ZnO particles had high crystallinity and were in the nanoscale range. The XRD pattern of Ag–ZnO also reveals the additional peaks of Ag–ZnO at 38° (111), 44.6° (200), and 64.1° (220), which correspond to cubic metallic Ag. The result indicated that Ag^{+} could get precipitated as an Ag metallic phase, confirming the successful formation of an Ag–ZnO nanocomposite. On the other hand, two extra peaks positioned at 28° (110) and 54.2° (211), which corresponded to tetragonal RuO_2 nanoparticles, could be observed for Ru–ZnO. No metallic Ru peak (Ru°) was detected by XRD analysis, which agrees well with the previous report (Bloh *et al.* 2014). The result confirmed the formation of ZnO with a small quantity of crystal RuO_2. The diameter of the ZnO crystallite was calculated using the Debye–Scherrer formula. The ZnO crystallite sizes were in order of ZnO (25.4 nm) < Ag–ZnO (29.8 nm) < Ru–ZnO (34.4 nm). Similar results were found in previous works showing

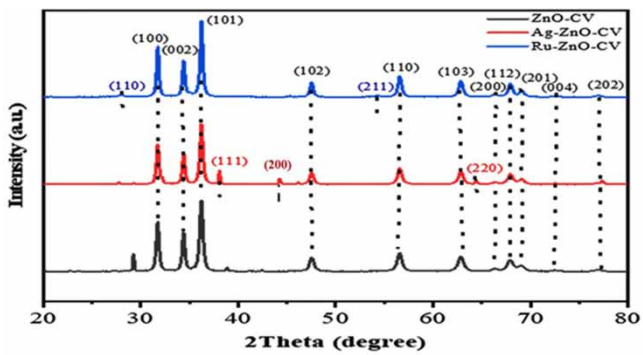

Figure 3 | XRD profiles of ZnO, Ag–ZnO, and Ru–ZnO nanocomposites synthesized by *C. viminalis* (CV) extract.

that the crystallite sizes of Ru–ZnO and Ag–ZnO were larger than those of pure ZnO (Aranganayagam *et al.* 2013; Nagaraju *et al.* 2017). An increase in crystallite size with Ag and Ru incorporation indicated ZnO lattice expansion.

An earlier report (Michael *et al.* 2014) suggested that noble metal can be incorporated into the ZnO crystal either as a substituent or as an interstitial atom, thereby introducing defects in the ZnO lattice. If Zn^{2+} is substituted by metal ions, a corresponding peak would be expected. However, no shift in the ZnO peaks was observed in the present study, which agrees with the previous work of Peng *et al.* (2019). Ag atoms can easily diffuse through the ZnO crystal structure and lead to implantation as Ag interstitial atoms (Masoumi *et al.* 2017). X-ray photoelectron spectroscopy (XPS) study previously confirmed the binding energies of metallic Ag in Ag–ZnO (Peng *et al.* 2019). On the other hand, the chemical oxidation states of Ru in the Ru–ZnO samples were investigated using the XPS technique (Manríquez *et al.* 2018). They found that two oxidation states exist on the surface of the Ru–ZnO solids: major Ru^{4+} (RuO_2) and minor Ru^{6+} (RuO_3). Several reports revealed that the Ru ions are incorporated into the ZnO lattice as either Ru^{6+} ions (Bloh *et al.* 2014), Ru^{4+} ions (Kumar *et al.* 2014), or Ru^{3+} ions (Aranganayagam *et al.* 2013). In the present work, the major oxidation state of the Ru ions in the Ru–ZnO nanocomposites is probably Ru^{4+} (RuO_2). RuO_2 was observed in XRD patterns, but other Ru species were not detected.

3.3. Morphology and nanostructure

Figure 4 shows TEM images of ZnO, Ag–ZnO, and Ru–ZnO samples. Clearly, the hexagonal-shaped ZnO nanoparticles were obtained together with the spherical Ag nanoparticles, as displayed in Figure 4(a) and 4(b). However, Ru–ZnO nanocomposites gave different nanostructures (Figure 4(c)). The formation of small clusters of tetragonal RuO_2 aggregates along with ZnO nanoparticles was present. The shapes of ZnO, Ag, and RuO_2 particles from TEM images are in good agreement with the XRD results. SAED of ZnO, Ag–ZnO, and Ru–ZnO are displayed in Figure 4(d)–4(f). The diffraction pattern shows that the pure ZnO nanoparticles and ZnO-based nanocomposites have different crystal orientations. The SAED pattern shows the characteristic ring of polycrystalline ZnO nanoparticles (Figure 4(d)). The Ag–ZnO nanocomposites were well crystallized in nature (Figure 4(e)). In Figure 4(f), the ring of the diffraction pattern diminishes with the addition of Ru metal, indicating that the crystallinity of ZnO nanoparticles decreases in Ru–ZnO. These results showed that, with the same synthesis procedure, different noble metals gave different crystallinities to the ZnO-based nanocomposite produced. Incorporation of Ru metals substantially decreased the crystallinity of the ZnO-based nanocomposites, whereas Ag metal retained the crystallinity of the ZnO-based nanocomposites.

Figure S1 presents FESEM images of the pure ZnO and Ag/ZnO nanocomposites. The spherical or block-like morphology, having approximately less than 100 nm in size with a smooth surface, was shown. Contrary to this, Ru–ZnO nanocomposites showed an irregular shape and tended to agglomerate in plagues. The particle size of Ru–ZnO was greater than that of pure

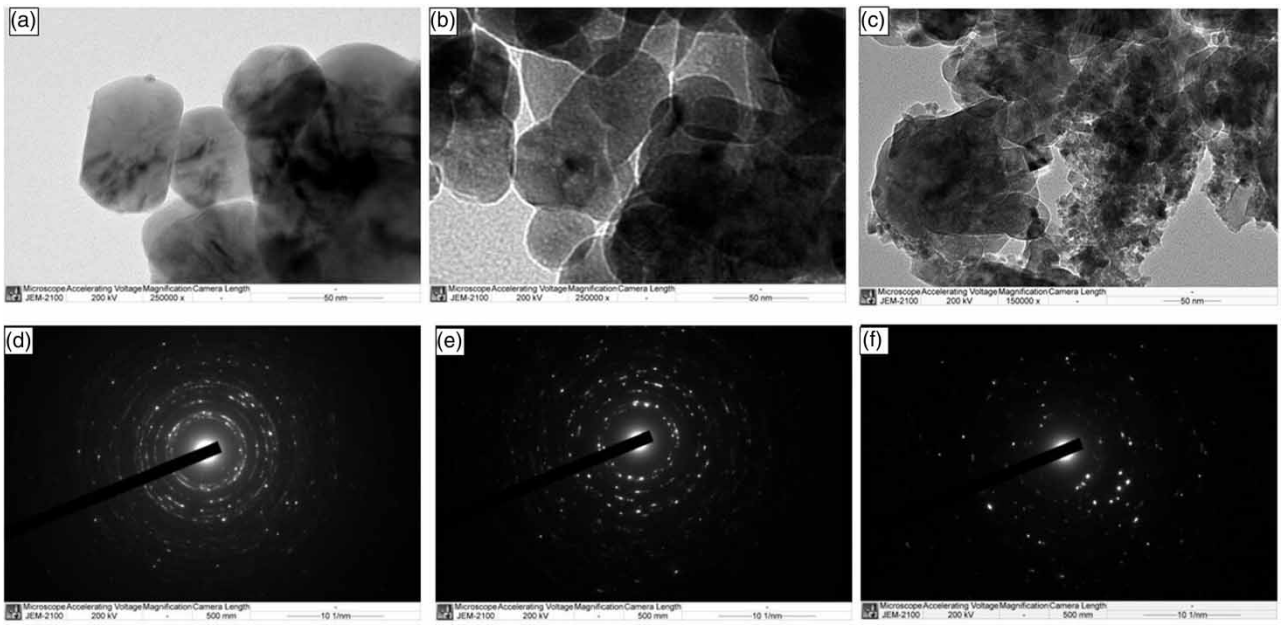

Figure 4 | TEM images and SAED patterns of (a,c) ZnO, (b,e) Ag–ZnO, and (c,f) Ru–ZnO.

ZnO and Ag–ZnO. This is probably due to the aggregation of RuO_2 on the surface of ZnO nanoparticles. The EDS spectra indicated that ZnO is the host material for Ag–ZnO and Ru–ZnO nanocomposites. The weight percentages of Ag and Ru elements achieved from the EDS studies were 17.07% Ru and 4.30% Ag (Figure S1).

3.4. FTIR spectra

Figure 5 shows the FTIR spectra of leaf extract, ZnO, Ag–ZnO, and Ru–ZnO nanocomposites. Various functional groups present in the CV leaf extract are seen. A significant vibration band at 3,300 cm^{-1} is assigned to the stretching vibration of the hydroxyl group (O–H) of phenolic compounds. A vibration band ranging from 2,800 to 2,900 cm^{-1} is assigned to the stretching vibration of the C–H of alkyl groups. A vibration band ranging from 1,700 to 1,750 cm^{-1} is assigned to the stretching vibration of the carbonyl group (C = O). A vibration band ranging from 1,600 to 1,650 cm^{-1} is assigned to the stretching vibration of the C = C group in aromatic rings. The FTIR spectra of CV extract indicated the presence of polyphenols and flavonoids. Flavonoids and phenols are involved in the stabilization, formation, and bioreduction of metal oxides and metal nanoparticles (Basnet *et al.* 2018).

Figure 5 displays the FTIR spectra of CV-mediated ZnO, Ag–ZnO, and Ru–ZnO samples. This was attributed to the interaction between functional groups in CV extract and prepared metal oxides. Noticeable vibration bands of biosynthesized ZnO were observed at 835, 840, and 1,355 cm^{-1}, whereas Ag–ZnO and Ru–ZnO nanocomposites had slightly different peaks at 696, 840, 1,153, 1,409, and 1,427 cm^{-1}. The bands at 1,355, 1,409, and 1,427 cm^{-1} were assigned to the hydroxyl group (O–H bonds), which indicates the presence of O – H bending vibration in phenolic compounds absorbed onto the metal oxide surface. Additionally, the vibration peaks at 1,153 cm^{-1} (C–O bonds), 835 and 840 cm^{-1} (C = C bonds), and 696 cm^{-1} (C–H bonds) were presented. The interaction between biological molecules and a metal oxide surface can create a layer that prevents agglomeration and increases the stability of nanoparticles (Faisal *et al.* 2021).

3.5. UV-Vis spectra

The UV-Vis absorption spectra of ZnO, Ru–ZnO, and Ag–ZnO are shown in Figure 6. The UV-Vis spectrum of ZnO consisted of an intense peak at 377 nm, whereas those of Ag–ZnO and Ru–ZnO nanocomposites showed an intense peak at 383 nm. The red shift confirmed the existence of the metals in the ZnO lattice and their interfacial effect on the ZnO surface (Adeel *et al.* 2021; Modwi *et al.* 2021). The red shift that led to the band gap lowering was a result of the gap level creation between the VB and CB of the ZnO nanoparticles by noble metals (Modwi *et al.* 2021). The band gap energies are calculated as 3.28, 3.23, and 3.23 eV for ZnO, Ag–ZnO, and Ru–ZnO, respectively. The narrowing of the band gap is good for photocatalytic activity as the energy demand to generate electron transfer from VB to CB decreases.

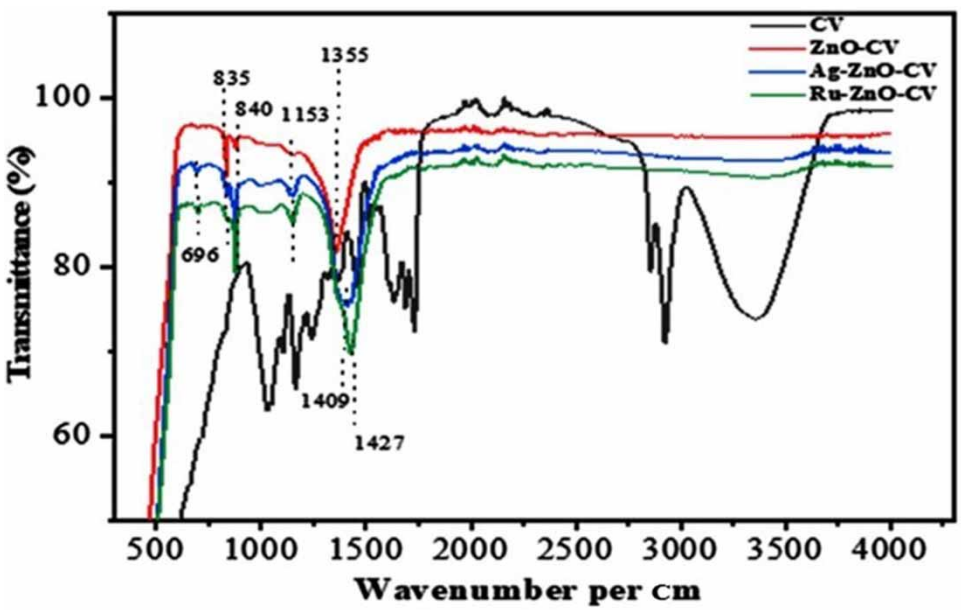

Figure 5 | FTIR spectra of biosynthesized ZnO, Ag–ZnO, and Ru–ZnO, and *C. viminalis* leaf extract.

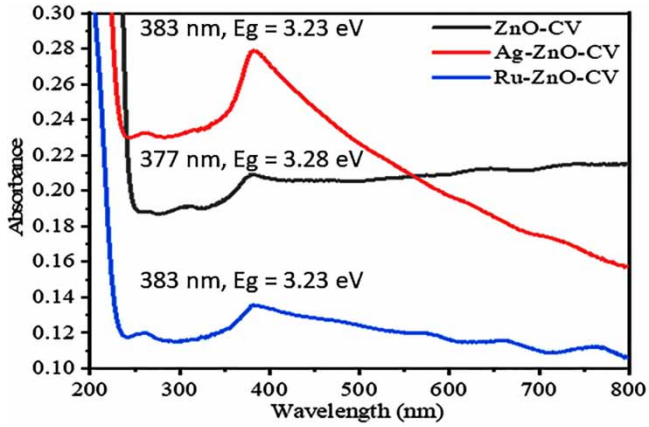

Figure 6 | UV-VIS spectra of biosynthesized ZnO, Ag–ZnO, and Ru–ZnO nanocomposites.

The incorporation of Ag during the ZnO synthesis process caused an increase in the absorbance value of Ag–ZnO in comparison to pure ZnO (Figure 6). A similar result was reported in a previous study (Kadam *et al.* 2018). The maximum adsorption value depends on the surface plasmon resonance (SPR) (Zare *et al.* 2019). Furthermore, a broad peak of Ag–ZnO was reported due to a plasmon band of Ag atoms, or a cluster of Ag atoms located on the surface of ZnO nanocrystals (Michael *et al.* 2014). Conversely, the addition of Ru caused a negative effect on the UV absorption of Ru–ZnO. This showed that the noble metals have a substantial effect on the optical properties of ZnO. The UV absorption capacity was found to be in the order Ag–ZnO > ZnO > Ru–ZnO. UV absorption is a first step in the semiconductor photocatalysis process. If Ru–ZnO exhibited poor UV absorption, the activation of the Ru–ZnO photocatalyst would be less.

3.6. Photocatalytic degradation of MB

ZnO can absorb UV light with a wavelength equal to or less than 385 nm to produce $^{\bullet}OH$ radicals, which attack the pollutants adsorbed on the surface of ZnO (Moezzi *et al.* 2012). Çifçi *et al.* (2016) reported that UVB irradiation (315 nm) provided a faster photocatalytic reaction rate than that under UVA irradiation. However, in the present work, the biosynthesized ZnO, Ag–ZnO, and Ru–ZnO samples exhibited good absorbance for UVA, but poor absorbance for UVB wavelengths (Figure 6). The photodegradation of MB dye was done under UV-A irradiation because of the strong absorbance of ZnO, Ag–ZnO, and Ru–ZnO at the UVA wavelength (Figure 6).

The photocatalytic degradation of MB under UVA irradiation is presented in Figure 7(a). The reduction of MB was found to be in the order Ag–ZnO > Ru–ZnO > ZnO. The photodegradation efficiencies were 94, 82, and 73% for Ag–ZnO,

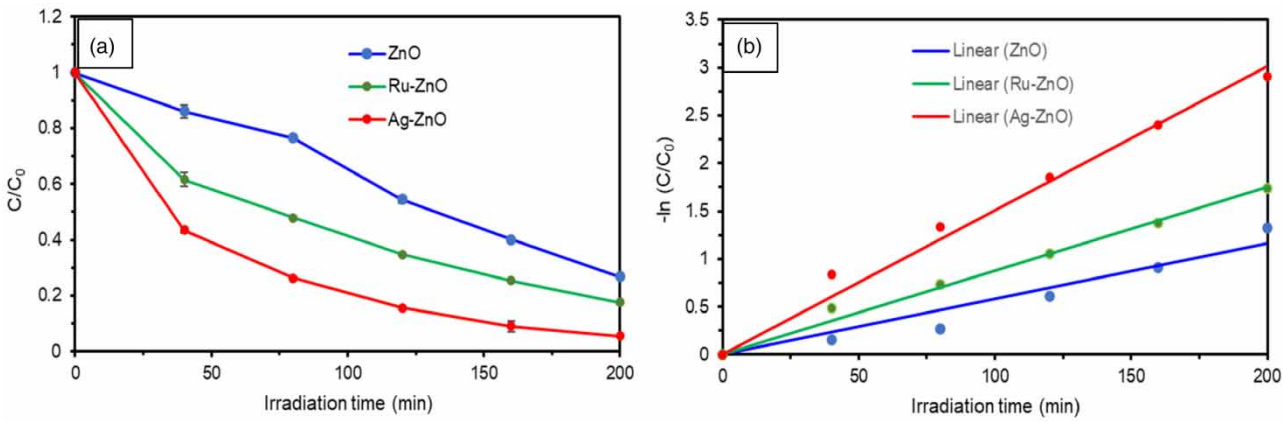

Figure 7 | (a) Time-dependent photodegradation and (b) the pseudo-first-order kinetics of MB dye degradation under UVA irradiation with ZnO, Ru–ZnO, and Ag–ZnO nanocomposites.

Ru–ZnO, and ZnO, respectively (Table 1). The pseudo-first-order rate constant (k) (min^{-1}) can be estimated using the slope of the line from Figure 7(b). The k values increased from 0.0058 of ZnO to 0.0088 min^{-1} of Ru–ZnO and to 0.0151 min^{-1} of Ag–ZnO, respectively (Table 1). The incorporation of Ru and Ag into the ZnO results in an increase in reaction rate, with the highest value being obtained for Ag–ZnO. The results showed the benefit of Ag incorporation for ZnO over Ru incorporation.

Modification of ZnO with noble metals effectively inhibits electron–hole recombination and thereby prolongs the lifetime of the electron–hole pairs and increases the amount of $^{\cdot}O_2^-$ and $^{\cdot}OH$ radicals (Fang *et al.* 2020). The present study first revealed the excellent photocatalytic performance of Ag–ZnO over Ru–ZnO. This might be attributed to the higher crystallinity, greater UV light adsorption capacity, and smaller particle sizes of biosynthesized Ag–ZnO, as shown in Figures 4, 6, and S1. High crystallinity of ZnO resulted in more generation of e–h pairs because of more adsorption of photons, and smaller particle sizes could generate more active sites for dye absorption and degradation (Supin *et al.* 2023).

Peng *et al.* (2019) investigated the role of active species ($^{\cdot}OH$ and $^{\bullet}O_2^-$) in the photocatalytic degradation of phenol over ZnO and Ag/ZnO using electron paramagnetic resonance (EPR) and quenching tests. They found that the intensity of $^{\cdot}OH$ and $^{\bullet}O_2^-$ signals in energy dispersive spectroscopy (EDS) spectra was significantly increased in Ag–ZnO in comparison to ZnO, which was consistent with the photocatalytic activity. The quenching test using the scavengers for $^{\cdot}OH$ and $^{\bullet}O_2^-$ revealed both $^{\cdot}OH$ and $^{\cdot}O_2^-$ contributions to the decomposition of phenol (Peng *et al.* 2019). On the other hand, Ding *et al.* (2020) reported that the EPR spectra of Ag/ZnO showed the existence and abundance of •OH radical peaks, whereas the $^{\cdot}O_2^-$ radical peak was not clear and insufficient, and the results all corresponded to quenching experiments. They suggested that the $^{\cdot}OH$ radical might play a more critical role than $^{\bullet}O_2^-$ in the photocatalytic degradation of metronidazole as an antimicrobial drug for Ag/ZnO.

3.7. Photocatalytic disinfection

The photocatalytic disinfection experiment was performed against *E. coli* present in the hospital wastewater (Figure 8). For pure ZnO, the *E. coli* population seemed to remain constant after 60 min of UVA light. This suggested that the *E. coli* present in the hospital wastewater are resistant to low photocatalytic activity by pure ZnO nanoparticles. Figure 8(a) shows the photocatalytic disinfection of *E. coli* at each irradiated time using ZnO, Ru–ZnO, and Ag–ZnO under UVA irradiation. The photocatalytic disinfection of ZnO was found to be negligible for the reduction

Table 1 | The efficiency and k values for each condition

	MB degradation			*E. coli* disinfection		
Condition	**Efficiency (%)**	**k (min^{-1})**	**R^2**	**Efficiency (%)**	**k (min^{-1})**	**R^2**
ZnO	73.27	0.0058	0.974	9.85	0.0020	0.967
Ru–ZnO	82.43	0.0088	0.997	34.98	0.0068	0.951
Ag–ZnO	94.55	0.0151	0.996	75.37	0.0193	0.949

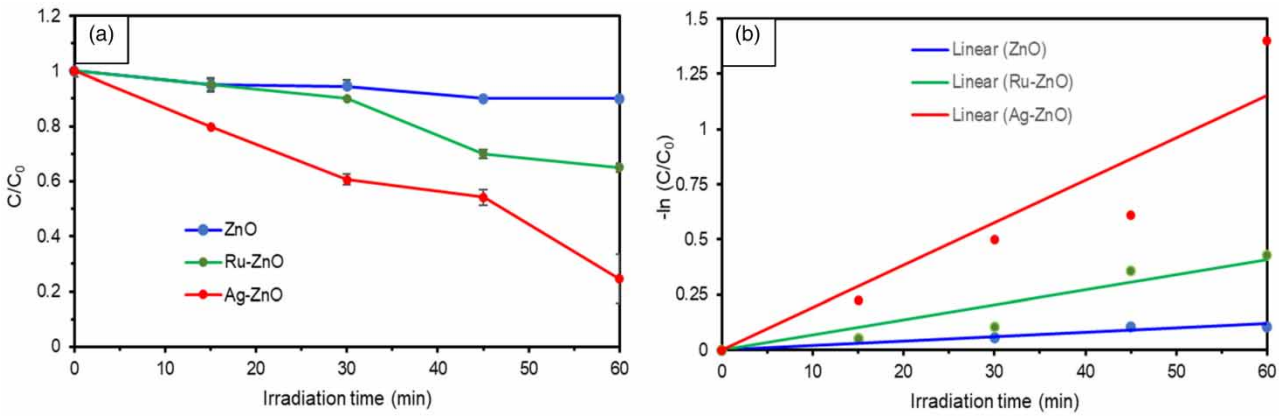

Figure 8 | (a) Time-dependent photocatalytic disinfection and (b) the pseudo-first-order kinetics of *E. coli* present in the hospital wastewater under UVA irradiation with ZnO, Ru–ZnO, and Ag–ZnO nanocomposites.

of the *E. coli* population. This suggests that the *E. coli* present in hospital wastewater are resistant to UVA light and ZnO. One possibility is that the amounts of $^{\cdot}O_2^-$ and $^{\bullet}OH$ produced on the surface of pure ZnO might be too low for the inactivation of *E. coli*. The $^{\bullet}OH$ radical is assumed to be the main reactant for the photocatalytic oxidation process, in which the amount of OH radical generation is correlated with the photocatalytic reactivity (Nosaka & Nosaka 2016). The diffusing $^{\bullet}OH$ radicals play an important role in photocatalytic disinfection (Zhang *et al.* 2010). The $^{\bullet}OH$ radicals have a pivotal impact on the cell membrane, thereby modifying the bacterium's metabolic activities and causing the inactivation of the bacterium (Saravanan *et al.* 2021).

The Ag–ZnO exhibited the highest photocatalytic disinfection among those prepared samples. The improved photocatalytic disinfection of Ag–ZnO can be attributed to multiple synergistic effects of greater UV absorption capacity, better charge carrier separation, and additional antimicrobial Ag ability that effectively kills the bacterial population near it (Matai *et al.* 2014). A kinetic reaction was studied using the pseudo-first equation model. Experimental values were fitted and shown in Figure 8(b). The linear relationship indicates that the photocatalytic disinfection of *E. coli* follows a pseudo-first order. The k values of ZnO, Ru–ZnO, and Ag–ZnO were found to be 2.0×10^{-3}, 6.8×10^{-3}, and 19.3×10^{-3} min^{-1}, respectively (Table 1). The highest photocatalytic performance was observed for Ag–ZnO, with a rate constant nine times higher than that of ZnO and two times higher than that of Ru–ZnO. The photocatalytic disinfection efficiencies for ZnO, Ru–ZnO, and Ag–ZnO during 60 min of illumination with UVA light were 9.85, 34.98, and 75.37%, respectively.

3.8. Antimicrobial activity in the dark

Table 2 shows the inhibition zones of ZnO, Ru–ZnO, and Ag–ZnO against *E. coli*. Results show that ZnO and Ru–ZnO could not develop zones of inhibition at both concentrations (1 and 10 mg/mL). The significant antimicrobial activity of Ag–ZnO was comparable. Ag–ZnO exhibited strong activity against *E. coli* when increasing its concentration from 1 to 10 mg/mL. This suggests that Ag–ZnO can be applied without UVA irradiation for the inactivation of *E. coli* present in hospital wastewater, but it requires a high dosage (10 mg/mL). Therefore, Ag NPs could be responsible for the antibacterial action of Ag–ZnO because no inhibition of *E. coli* was found for ZnO NPs (Table 2). The development of an inhibition zone for high-dose Ag–ZnO is probably attributed to the increased antimicrobial effect of Ag NPs on the surface of ZnO. This result also suggested the resistance of *E. coli* in hospital wastewater to ZnO. On the other hand, the effect of Ag NPs against multi-drug-resistant *E. coli* was also reported (Selem *et al.* 2022).

The antimicrobial performance of Ag–ZnO with and without UVA irradiation was observed based on the ISO 27447 standard test method. Table 3 shows that the percentage reduction of hospital wastewater *E. coli* after exposure to Ag–ZnO

Table 2 | Zone of inhibition by different nanomaterials on hospital wastewater *E. coli* bacteria

	Samples concentrations	
Samples	**1 mg/mL**	**10 mg/mL**
ZnO	0 mm	0 mm
Ag/ZnO	0 mm	12 ± 0 mm
Ru/ZnO	0 mm	0 mm

Table 3 | Percent reduction of *E. coli* using ZnO, Ag–ZnO, and Ru–ZnO with and without UVA light

	In the dark			Under UVA irradiation		
	Number of *E. coli* (× 10^4 CFU/mL)			Number of *E. coli* (× 10^4 CFU/mL)		
Sample	**0 h**	**8 h**	**% reduction**	**0 h**	**8 h**	**% reduction**
ZnO	4.04	3.34 ± 0.05	17.3	4.04	0.27 ± 0.01	93.3
Ru–ZnO	4.04	2.80 ± 0.07	30.7	4.04	0.18 ± 0.01	95.5
Ag–ZnO	4.04	2.21 ± 0.42	45.3	4.04	0.003 ± 0.00	99.9

immobilized on filter paper for 8 h. The *E. coli* reduction efficiency was two times lower in the dark than that in the presence of UVA light. Under UVA irradiation, the reactive species play a dominant role in the photocatalytic disinfection process (Saravanan *et al.* 2021). The synergistic effect of reactive species (.OH) and Ag NPs on the surface of Ag–ZnO might considerably cause cell membrane damage, thereby automatically enhancing the inactivation of *E. coli*.

4. CONCLUSIONS

The present study aimed to investigate the effect of different noble metals on the characteristics and photocatalytic disinfection of biosynthesized metal-ZnO nanocomposites. The binary ZnO-based nanocomposites with silver and ruthenium metals were synthesized using CV aqueous extract. Characterizations were accomplished using XRD, FTIR, UV-Vis, FESEM, EDS, TEM, and SAED techniques, confirming the formation of Ag–ZnO and Ru–ZnO nanocomposites. Ag–ZnO and Ru–ZnO had different nanostructures, crystallinities, UV adsorption capacities, and photocatalytic efficiency. Ag–ZnO and Ru–ZnO exhibited remarkably higher photocatalytic efficiency and reaction rate than those of ZnO. Furthermore, the photocatalytic activity was improved dramatically by metallic Ag rather than Ru/RuO_2. Results also indicated that Ag–ZnO could inactivate *E. coli* present in hospital wastewater via photocatalytic disinfection under UVA irradiation and Ag antimicrobial itself in the dark. This work indicates the advantage of the binary ZnO nanocomposite together with metallic Ag over Ru/RuO_2.

ACKNOWLEDGEMENTS

This study was supported financially by the National Nanotechnology Center, National Science and Technology Development, Thailand (Grant No. P1751698). We extremely thank the Thailand Graduate Institute of Science and Technology, National Science and Technology Development, Thailand, for supporting graduate student scholarships.

DATA AVAILABILITY STATEMENT

All relevant data are included in the paper or its Supplementary Information.

CONFLICT OF INTEREST

The authors declare there is no conflict.

REFERENCES

Abu-Sini, M. K., Maharmah, R. A., Abulebdah, D. H. & Al-Sabi, M. N. S. 2023 Isolation and identification of coliform bacteria and multidrug-resistant *Escherichia coli* from water intended for drug compounding in community pharmacies in Jordan. *Healthcare* **11** (3), 299. https://doi.org/10.3390/healthcare11030299.

Adeel, M., Saeed, M., Khan, I., Muneer, M. & Akram, N. 2021 Synthesis and characterization of Co – ZnO and evaluation of its photocatalytic activity for photodegradation of methyl orange. *ACS Omega* **6**, 1426–1435. https://doi.org/10.1021/acsomega.0c05092.

Ahmad, K. & Athar, F. 2017 Phytochemistry and pharmacology of *Callistemon viminalis* (Myrtaceae): a review. *The Natural Products Journal* **7**, 1–10. https://doi.org/10.2174/ 22103155076661612161O 0323.

Ahmed, S. N. & Haider, W. 2018 Heterogeneous photocatalysis and its potential applications in water and wastewater treatment: a review. *Nanotechnology* **29**, 342001. https://doi.org/10.1088/ 1361-6528/aac6ea.

Aranganayagam, K. R., Senthilkumaar, S., Subramanism, N. G. & Kang, T. W. 2013 Ruthenium doped ZnO semiconductor: synthesis, characterization and photodegradation of azo dye. *International Journal of Nanoscience* **12** (02), 1350009. https://doi.org/10.1142/S0219581X13500099.

Basnet, P., Chanu, T. I., Samanta, D. & Chatterjee, S. A. 2018 A review on biosynthesized zinc oxide nanoparticles using plant extracts as reductants and stabilizing agents. *Journal of Photochemistry and Photobiology B: Biology* **183**, 201–221. https://doi.org/10.1016/j.jphotobiol.2018.04.036.

Bloh, J. Z., Dillert, R. & Bahnemann, D. W. 2014 Ruthenium-modified zinc oxide, a highly active vis-photocatalyst: the nature and reactivity of photoactive centres. *Physical Chemistry Chemical Physics* **16**, 5833–5845. https://doi.org/10.1039/C3CP55136A.

Choi, Y. I., Jung, H. J., Shin, W. G. & Sohn, Y. 2015 Band gap-engineered ZnO and Ag/ZnO by ball-milling method and their photocatalytic and Fenton-like photocatalytic activities. *Applied Surface Science* **356**, 615–625. https://doi.org/10.1016/j.apsusc.2015.08.118.

Çifçi, D. I., Tunçal, T., Pala, A. & Uslu, O. 2016 Determination of optimum extinction wavelength for paracetamol removal through energy efficient thin film reactor. *Journal of Photochemistry and Photobiology A: Chemistry* **322–323**, 102–109. https://doi.org/10.1016/j.jphotochem.2016.03.003.

Ding, C., Fu, K., Pan, Y., Liu, J., Deng, H. & Shi, J. 2020 Comparison of Ag and AgI-modified ZnO as heterogeneous photocatalysts for simulated sunlight driven photodegradation of metronidazole. *Catalysts* **10**, 1097. https://doi.org/10.3390/catal10091097.

Dwivedi, P., Jatrana, I., Khan, A. U., Khan, A. A., Satiya, H., Khan, M., Moon, I. S. & Alam, M. 2021 Photoremediation of methylene blue by biosynthesized ZnO/Fe_3O_4 nanocomposites using *Callistemon viminalis* leaves aqueous extract: a comparative study. *Nanotechnology Reviews* **10**, 1912–1925. https://doi.org/10.1515/ntrev-2021-0117.

Faisal, S., Jan, H., Shah, S. A., Shah, S., Khan, A., Akbar, M. T., Rizwan, M., Jan, F., Wajidullah, Akhtar, N., Khattak, A. & Syed, S. 2021 Green synthesis of zinc oxide (ZnO) nanoparticles using aqueous fruit extracts of *Myristica fragrans*: their characterizations and biological and environmental applications. *ACS Omega* **6**, 9709–9722. https://doi.org/10.1021/ acsomega.1c00310.

Fang, L., Zhang, X., Xiang, J., Zhao, M., Zheng, B. & Bai, L. 2020 Solvent polarity resulted in different structures and photocatalytic abilities of Ag/ZnO composites. *Journal of Sol-Gel Science and Technology* **93**, 695–702. https://doi.org/10.1007/s10971-019-05181-2.

Kadam, A. N., Bhopate, D. P., Kondalkar, V. V., Majhi, S. M., Bathula, C. D., Tran, A.-V. & Lee, S.-W. 2018 Facile synthesis of Ag-ZnO core–shell nanostructures with enhanced photocatalytic activity. *Journal of Industry and Engineering Chemistry* **61**, 78–86. https://doi.org/10.1016/j.jiec.2017.12.003.

Kannan, S. K. & Sundrarajan, M. 2015 Green synthesis of ruthenium oxide nanoparticles: characterization and its antibacterial activity. *Advanced Powder Technology* **26**, 1505–1511. https://doi.org/10.1016/j.apt.2015.08.009.

Kumar, S., Kaur, P., Chen, C. L., Thangavel, R., Dong, C. L., Ho, Y. K., Lee, J. F., Chan, T. S., Chen, T. K., Mok, B. H., Rao, S. M. & Wu, M. K. 2014 Structural, optical and magnetic characterization of Ru doped ZnO nanorods. *Journal of Alloys and Compounds* **588**, 705–709. https://doi.org/10.1016/j.jallcom.2013.11.137.

Liu, H., Feng, J. & Jie, W. A. 2017 Review of noble metal (Pd, Ag, Pt, Au)–zinc oxide nanocomposites: synthesis, structures and applications. *Journal of Material Science: Materials in Electronics* **28**, 16585–16597. https://doi.org/10.1007/s10854-017-7612-0.

Maal, K. B., Delfan, A. S. & Salmanizadeh, S. 2015 Isolation and identification of two novel *Escherichia coli* bacteriophages and their application in wastewater treatment and coliform's phage therapy. *Jundishapur Journal of Microbiology* **8** (3), e14945. https://doi.org/10.5812/ jjm.14945.

Manríquez, M. E., Noreña, L. E., Wang, J. A., Chen, L., Salmones, J., González-García, J., Reza, C., Tzompantzi, F., Cortez, J. G. H., Ye, L. & Xi, H. 2018 One-pot synthesis of Ru-doped ZnO oxides for photodegradation of 4-chlorophenol. *International Journal of Photoenergy* **2018**, 7605306. https://doi.org/10.1155/2018/7605306.

Masoumi, S., Noori, A. & Nadimi, E. 2017 Diffusion mechanisms of Ag atom in ZnO crystal: a first principles study. *Journal of Physics: Conference Series* **939**, 012014. https://doi.org/ 10.1088/1742-6596/939/1/012014.

Matai, I., Sachdev, A., Dubey, P., Kumar, S. U., Bhushan, B. & Gopinath, P. 2014 Antibacterial activity, and mechanism of Ag–ZnO nanocomposite on *S. aureus* and GFP-expressing antibiotic resistant *E. coli*. *Colloids and Surfaces B: Biointerfaces* **115**, 359–367. https://doi.org/10.1016/j.colsurfb.2013.12.005.

Michael, R. J. V., Sambandam, B., Muthukumar, T., Umapathya, M. J. & Manoharan, P. T. 2014 Spectroscopic dimensions of silver nanoparticles and clusters in ZnO matrix and their role in bioinspired antifouling and photocatalysis. *Physical Chemistry Chemical Physics* **16**, 8541–8555. https://doi.org/10.1039/c4cp00169a.

Modwi, A., Mustafa, B., Ismail, M., Makawi, S. Z. A., Hussein, T. I., Abaker, Z. M., Mujawah, A. & Al-Ayed, A. S. 2021 Physicochemical and photocatalytic performance of the synthesized ruo_2-ZnO photo-composite in the presence of pectinose solution. *Environmental Nanotechnology, Monitoring & Management* **15**, 100403. https://doi.org/10.1016/ j.enmm.2020.100403.

Moezzi, A., McDonagh, A. M. & Cortie, M. B. 2012 Zinc oxide particles: synthesis, properties and applications. *Chemical Engineering Journal* **185–186**, 1–22. http://doi.org/10.1016/ j.cej.2012.01.076.

Muttaqin, R., Ratnawati, R. & Slamet, S. 2022 Batch electrocoagulation system using aluminum and stainless steel 316 plates for hospital wastewater treatment. *IOP Conference Series: Earth and Environmental Science* **963**, 012056. https://doi.org/10.1088/1755-1315/963/1/012056.

Nagaraju, G., Udayabhanu, S., Prashanth, S. A., Shastri, M., Yathish, K. V., Anupama, C. & Rangappa, D. 2017 Electrochemical heavy metal detection, photocatalytic, photoluminescence, biodiesel production and antibacterial activities of Ag–ZnO nanomaterial. *Materials Research Bulletin* **94**, 54–63. https://doi.org/10.1016/j.materresbull.2017.05.043.

Nosaka, Y. & Nosaka, A. 2016 Understanding hydroxyl radical (˙OH) generation processes in photocatalysis. *ACS Energy Letters* **1** (2), 356–359. https://doi.org/10.1021/acsenergylett. 6b00174.

Odonkor, S. T. & Addo, K. K. 2018 Prevalence of multidrug-resistant *Escherichia coli* isolated from drinking water sources. *International Journal of Microbiology* **19**, 7204013. https://doi.org/10.1155/2018/7204013.

Oluwole, A. O., Omotola, E. O. & Olatunji, O. S. 2020 Pharmaceuticals and personal care products in water and wastewater: a review of treatment processes and use of photocatalyst immobilized on functionalized carbon in AOP degradation. *BMC Chemistry* **14**, 62. https://doi.org/ 10.1186/s13065-020-00714-1.

Pathak, T. K., Kroon, R. E., Craciun, V., Popa, M., Chifiriuc, M. C. & Swart, H. C. 2019 Influence of Ag, Au and Pd noble metals doping on structural, optical and antimicrobial properties of zinc oxide and titanium dioxide nanomaterials. *Heliyon* **5** (3), e01333. https://doi.org/10.1016/j.heliyon.2019.e01333.

Peng, J., Lu, T., Ming, H., Ding, Z., Yu, Z., Zhang, J. & Hou, Y. 2019 Enhanced photocatalytic ozonation of phenol by Ag/ZnO nanocomposites. *Catalysts* **9**, 1006. https://doi.org/10.3390/catal9121006.

Poirel, L., Madec, J. Y., Lupo, A., Schink, A. K., Kieffer, N., Nordmann, P. & Schwarz, S. 2018 Antimicrobial resistance in *Escherichia coli*. *Microbiology Spectrum* **6** (4), ARBA-0026-2017. https://doi.org/10.1128/microbiolspec.arba-0026-2017.

Roy, N. & Chakraborty, S. 2021 ZnO as photocatalyst: an approach to wastewater treatment. *Materials Today: Proceedings* **46** (14), 6399–6403. https://doi.org/10.1016/ j.matpr.2020.06.264.

Sadeghfar, F., Ghaedi, M. & Zalipour, Z., 2021 Chapter 4 - Advanced oxidation. In: *Interface Science and Technology*, Vol. 32 (Ghaedi, M., ed.). Elsevier, pp. 225–324. https://doi.org/10.1016/B978-0-12-818806-4.00001-2

Salem, M. Z. M., EL-Hefny, M., Nasser, R. A., Ali, H. M., El-Shanhorey, N. A. & Elansary, H. O. 2017 Medicinal and biological values of *Callistemon viminalis* extracts: history, current situation and prospects. *Asian Pacific Journal of Tropical Medicine* **10**, 229–237. https://doi.org/10.1016/j.apjtm.2017.03.015.

Saravanan, A., Kumar, P. S., Jeevanantham, S., Karishma, S. & Kiruthika, A. R. 2021 Photocatalytic disinfection of micro-organisms: mechanisms and applications. *Environmental Technology & Innovation* **24**, 101909. https://doi.org/10.1016/j.eti.2021.101909.

Selem, E., Mekky, A. F., Hassanein, W. A., Reda, F. M. & Selim, Y. A. 2022 Antibacterial and antibiofilm effects of silver nanoparticles against the uropathogen *Escherichia coli* U12. *Saudi Journal of Biological Sciences* **29** (11), 103457. https://doi.org/10.1016/j.sjbs.2022.103457.

Shintre, S. N., Wadhai, S. & Thakur, P. 2022 Synthesis of Ag/ZnO-AC composite photocatalyst: spectroscopic investigation, parameter optimization, synergistic effect, and performance enhancement for cost-effective photocatalytic degradation of phenols and dyes. *Water Science and Technology* **85** (9), 2663. https://doi.org/10.2166/wst.2022.137.

Supin, K. K., Namboothiri, P. P. M. & Vasundhara, M. 2023 Enhanced photocatalytic activity in ZnO nanoparticles developed using novel *Lepidagathis ananthapuramensis* leaf extract. *RSC Advances* **13**, 1497–1515. https://doi.org/10.1039/D2RA06967A.

Zare, M., Namratha, K., Alghamdi, S., Mohammad, Y. H. E., Hezam, A., Zare, M., Drmosh, Q. A., Byrappa, K., Chandrashekar, B. N., Ramakrishna, S. & Zhang, X. 2019 Novel green biomimetic approach for synthesis of ZnO-Ag nanocomposite; antimicrobial activity against food-borne pathogen, biocompatibility and solar photocatalysis. *Scientific Report* **9**, 8303. https://doi.org/10.1038/s41598-019-44309-w.

Zhang, L.-S., Wong, K.-H., Yip, H.-Y., Hu, C., Yu, J. C., Chan, C.-Y. & Wong, P.-K. 2010 Effective photocatalytic disinfection of *E. coli* K-12 using AgBr-Ag-Bi_2WO_6 nanojunction system irradiated by visible light: the role of diffusing hydroxyl radicals. *Environmental Science & Technology* **44**, 1392–1398. https://doi.org/10.1021/es903087w.

Zhang, S., Huang, J., Zhao, Z., Cao, Y. & Li, B. 2020 Hospital wastewater as a reservoir for antibiotic resistance genes: a meta-analysis. *Frontier in Public Health* **28** (8), 574968. https://doi.org/10.3389/fpubh.2020.574968.

First received 14 May 2023; accepted in revised form 11 August 2023. Available online 25 August 2023